9th ECCOMAS Thematic Conference on the Mechanical Response of Composites
COMPOSITES 2023
G. Catalanotti, H. Petterman and G. Pittaresi (Eds)

# SHM SYSTEM FOR BONDING LINE MONITORING OF COMPOSITE WING BOX SKIN-SPAR CAP DURING MANUFACTURING

**M. Ciminello[1*], A. Concilio[1], U. Mercurio[2] and G. Apuleo [3]**

[1]Adaptive Structures Division, The Italian Aerospace Research Centre (CIRA), 81043 Capua, Italy;
[2]Aeronautical Technology Integration Unit, The Italian Aerospace Research Centre (CIRA), 81043
[3] Research Division, Piaggio Aerospace Industries, 81043 Capua, Italy
*m.ciminello@cira.it

**Keywords:** SHM, Experimental validation, Industrial applications

**Summary:** *The CFRP wing box section under investigation is a stringer less wing-box (develop within the OPTICOMS research project) and consists of two portions: an upper part, made of co-cured spars and a top skin panel, and a bottom cured skin panel. The two portions are joined with a bonding process, giving rise to the final wing-box. During that final assembly step, distributed fibre optics were embedded between the spar caps and the bottom skin panel along the bonding lines. The embedded FO consists of six distributed fibres running within the bonding layer for about 1 m along the span direction. An irregular damage map was defined, by simulating the presence of manufacturing bonding defects by the intersection of teflon patches, different for width and length, to check an SHM system capabilities in detecting such flaws. The SHM system was tested after the final bonding process, by exploring the info contained within the "residual strains" data of the unloaded structure. Results obtained by post processing data for each fibre optic, are reported. The damage index associated to the eligible sensors is provided. Based on the available data, the SHM algorithm appeared to be sensible enough to hundreds of microstrain signals. Concerning faults detection, sensor density seems a key. Errors in the estimate of the damage extension can be assessed to be around 25%.*

## 1 INTRODUCTION

One of the expectations for an SHM system is to be qualified as a repeatable and reliable non-destructive inspection technique, as the ones that are referred to in many standards and regulations. This may be particularly important for bonded structures. While the associated technology may actually lead to relevant advantages in reducing weight and manufacturing times, the current protocols are very, and reasonably, stringent for bonded joints the failures of which may result in the catastrophic loss of the aircraft. In that case, it is in fact required that the construction is capable to bear the design limit load in correspondence of the maximum debonding occurrences allowed from the design characteristics using some stop debonding solutions like fasteners. Alternatively, it may be chosen to let any bonded critical joints undergo experimental verification test at limit load. Clearly, this is not viable for any aeronautic vehicle that is produced in series for the extremely huge associated costs. As a last possibility, it is cited in the airworthiness rules that would be acceptable the use of verified and reliable non-destructive inspection techniques, or NDI, able to guarantee the strength of the investigated

critical bonded joints. In the mentioned perspective, SHM system can target that aim considering no conventional current NDT method can be used to measure bond-line quality, due to the phenomenon of a "kissing bond". In this context, the adoption of an SHM system to detect damage and/or changes in the health status of a structure is proving successful due to its peculiarity of fully integration capability [1-3].

Among the available SHM technologies, valuable for the mentioned applications, the use of distributed fibre optics sensing [4], or multiplexed Fibre Bragg Gratings [5], appears by years quite attractive. If airborne applications are explored, at the current status of the technology, the second ones shall be preferred since these latter may count on interrogators that can be embarked, without being affected by the harsh environment of the flight, or giving effect to the on-board electronics. In the aerospace field, Fibre Optic Sensors, (FOS), lead to many other advantages, which conventional alternatives have not: they are quite flexible, tolerant to environmental conditions, and almost transparent to electromagnetic interferences. Finally, their transversal section allows easy embedding within large composite-material-based structural components, such as many current wings, [6]. Examples of in-flight applications can be easily found in literature: for instance, embedded FBG sensors were successfully applied on the Nishant, an Indian UAV [7].

The SHM technique herein proposed is based on distributed FOS; on that architecture, CIRA developed a dedicated algorithm (LHEO), to identify the damage location and size [8-10] along the skin-spar cap bonding lines of a composite wing box during the manufacturing.

This work was carried out and funded within the European Union program Clean Sky 2 AIR ITD WP B1.2 (Grant Agreement n°: 945521 CS2-AIR-GAM-2020) and the Clean Sky2 project OPTICOMS. The SHM system herein described based on FBGs embedded along skin/spar cap bonding lines will be implemented in the final 7m wing box final structural ground demonstrator of the OPTICOMS project for the its validation at full scale level.

## 2 THE STRUCTURAL COMPONENT

The test article, manufactured by the OPTICOMS consortium, is a segment between the stations at BL=4000 mm and BL=5200 mm of the Piaggio P180 wing. Such a wing segment is composed of skins, ribs and spars made of Carbon Fibre Reinforced Polymer (CFRP) material; spars, ribs, and the top skin panel are co-cured together (Figure 1), plus a bottom panel, added in a second curing step, at room temperature (Figure 2). One of the main features of such a wing-box section is to have a middle spar running only partially along its span. The length of the wing-box is about 1.2 m, while the root and tip chords are about 0.57 and 0.49 m, respectively. Fibre optic lines are tracked in yellow along the spar caps (Figure 1).

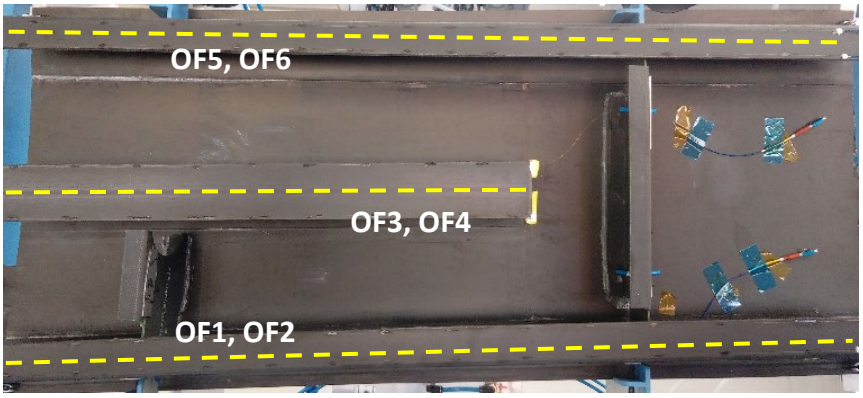

Figure 1: The upper skin with co-cured spar and the sensor system layout track.

An irregular damage map was defined on the bottom panel. Faults were different for width and length, to check algorithm capabilities in individuating such flaws under typical qualification loads (compression and bending up to limit load) and also under other particular conditions, i.e. after curing.

The damage map is visible in Figure 2, corresponding to the areas where Teflon patches were placed within selected areas on the spar caps. The main idea was to simulate the presence of disbonded areas, therefore characterized by a lower mechanical strength.

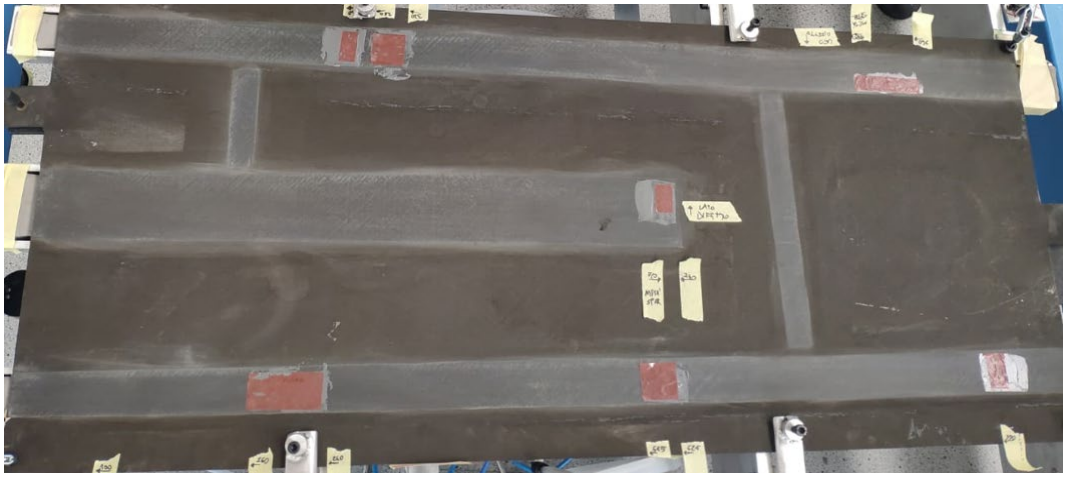
Figure 2: The lower skin with the Teflon tape simulating a disbonded area.

The SHM system was tested on the manufactured unloaded item, soon after the final curing process, by exploring the info contained within the so-called “residual strains” (in Figure 3, an overall view of the CAD of the parts of the structural components is reported). It was in fact considered that, during curing, the structural system would have experienced some thermal and even unwanted pre-stresses.

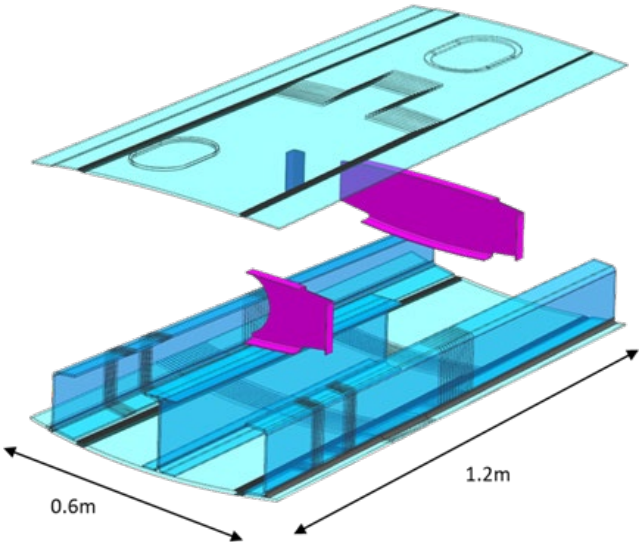


Figure 3: The CAD of the main structural components.

To face this target, distributed FOS were embedded within the bonding lines during the assembly. A total number of 6 OF (Optical Fibres) were placed. The process of mounting the fibre optic strain sensor is very similar to the process of mounting electrical foil strain gages. The same surface preparation methods are used and similar adhesive selection considerations are made. These measurements concern the strains in the direction of the fibre sensor. Therefore, in order to capture strain at the location(s) and in the direction(s) of interest on the test article, it is important to plan the sensor route (Figure 4).

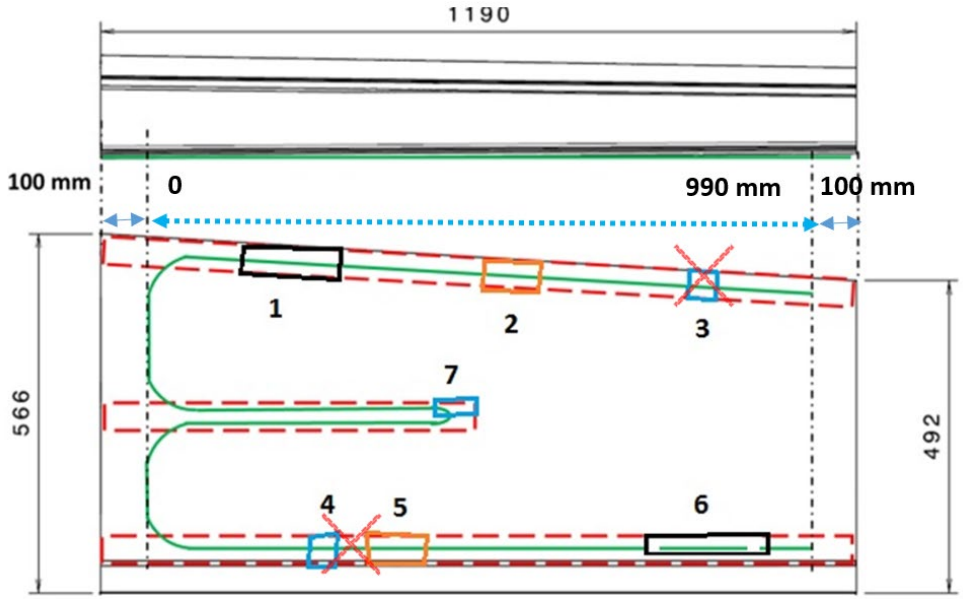


Figure 4: The sketch of a possible distributed fibre optic route layout on the investigated structural component and the defined damage map. The dotted rectangle indicates the region of interest far from the cradle area. In addition, there are two flags on damage 3 and damage 4-5. The reason is that damage 3 was discovered to be bonded out of the region of interest, while damage 4-5 were merged due to the resin squeezing post assembly.

In order to prevent fibre breakage during manufacturing, transportation and testing (considering potting both the wing box edges), and according to the previous considerations about

sensors installation, a scheme (Figure 5) was provided for the egress of the fibre leads. Depending on the manufacturing process, before the vacuum bag and curing, it is possible to leave the fibre connector outside the vacuum bag, and sealing the loose tube to the bag by using a tacky tape; it is also useful to apply a breeder layer all over the external fibre tubing/connector in order to prevent the vacuum can overpressure it.

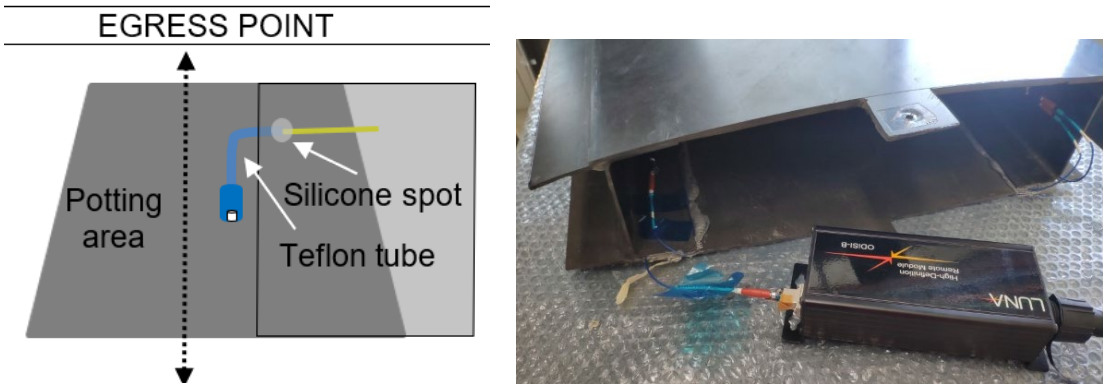


Figure 5: The 1egress of the fibre lead: left) sketch for the lead; right) egress point after manufacturing.

The test article was then supplied to PAI (Piaggio Aero Industry) test laboratory, with the optical fibres already installed. Strain gauges and cradle mounting were installed “in situ” at the test laboratory premises (Figure 6).

Figure 6: The wing box installed on the test rig in Piaggio Lab.

In what follows the SHM methodology is introduced and the monitoring of the unloaded structure is provided.

## 3 SHM METHODOLOGY

The LHEO (Local High-Edge Observation) algorithm tries to consider structural damage as an edge discontinuity along the strain energy signature. Its logic diagram is reported in Figure 7. The core of the methodology is the cross-correlation function.

For the sake of clarity, the cross-correlation function [9,10] represents the measure of similarity of two signals as a function of a time shift or a spatial translation applied to one of them.

$$R_{ij}(t) = \frac{1}{N}\sum_{l=0}^{N-1} x_i(t)x_j(t+\tau) \tag{1}$$

where N is the sample number of structural responses, τ is the time delay; if i=j, Eq. (1) is the auto-correlation function. Considering two real-valued signals (the i-th and the j-th) and a generic x-axis, (whatever the variable x may represent), the cross-correlation can be calculated to show how much the i-th signal must be anticipated along the x axes, to make it identical to the reference j-th one.

The formula anticipates the signal along the axis, by calculating the integral of the product for each possible value of the displacement. By considering strain measurements as input signals, the cross-correlation function of Eq. (1), can be written by using Eq. (2) as follows:

$$R_{ij}(t) = \frac{1}{N}\sum_{l=0}^{N-1} \varepsilon_i(t)\varepsilon_j(t+\Delta\tau) \tag{2}$$

(some expressions of the cross-correlation function may include a multiplying constant referring to the input force that can be eliminated by normalizing with its root mean square value). By setting the maximum value of the auto-correlation envelope function of the current responses as a vector:

$$R_{max}(t) = [max(R_{ii}(T))] \tag{3}$$

where $i = 1, 2, \ldots, n$, is the response from measurement sensor point i. The relative change of cross-correlation function with respect to the reference auto-correlation vector Eq. (4), is defined as:

$$DI_i = [(R_{ij})] - [R_{max}] \tag{4}$$

In the absence of a jump/edge, the cross-correlation variance with respect to autocorrelation will be small. On the contrary, if an edge is present, the two function values will be quite different. In the next paragraph, the strain data elaboration from unloaded structural condition just after the curing process of the test article, is reported.

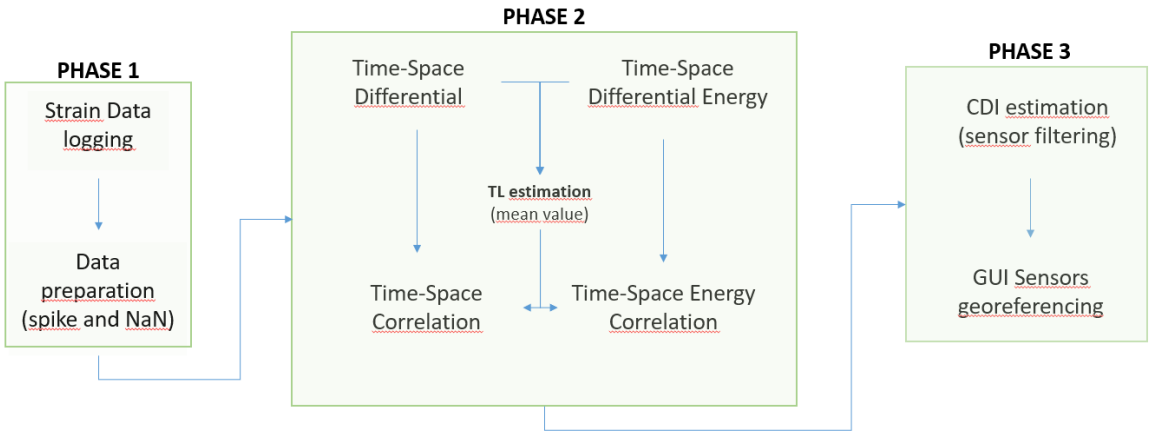


Figure 7: The logic diagram of the SHM methodology.

## 5 RESULTS

In what follows, the residual strain is compared in two different conditions. The first one just after the assembly of the wing box, and the second one after the wing box was delivered in the Piaggio Labs and installed on the test rig. The wing box was unloaded and simply supported in the first case, while in the installation it assumed a cantilever beam-like configuration.

The ODiSI B by Luna Inc., was used during this application, to provide measurements along the entire length of a fibre at a millimetre-scale sensor spacing. The Figure 8 shows a comparison between the strain distribution at assembly (black curve) and at installation (red curve) phases. The plots refer to the fibre OF1, bonded on the rear spar, and the fibre OF5 bonded on the front spar.

A non-zero strain map is revealed, much more evident after the installation on the test rig. Indeed, the cantilever beam-like configuration on the test rig added a gravity load over the span of the box providing a strain shift of the overall signal. In addition, the strain distribution also showed a clear compression effect in the area of the cradle (indicated by a red arrow). Finally, the effective length of the fibre optic along the spar is retrieved, by marking the abscissa (black arrows) corresponding to the egress point on the connector side.

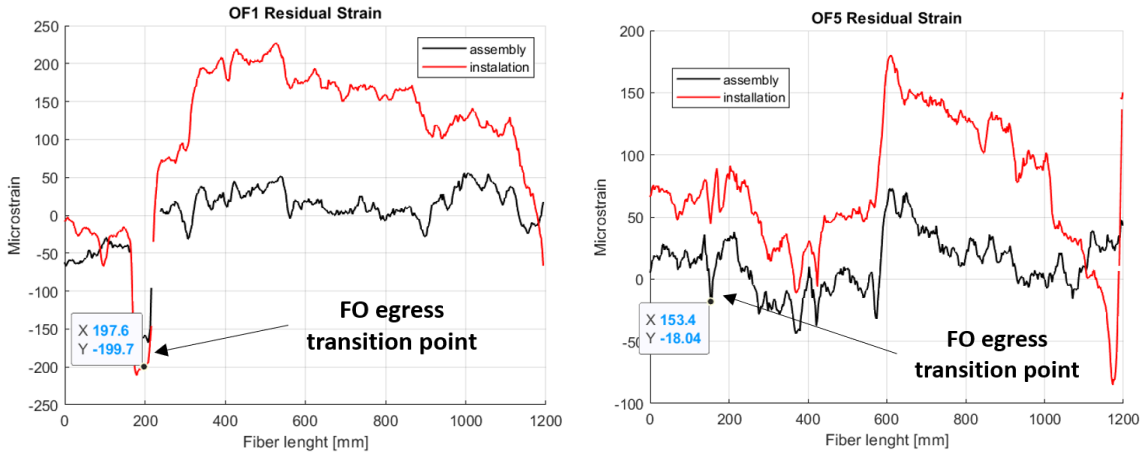


Figure 8: The residual strain after assembly (black line) and after installation on the test rig (red line).

In the next figures, the post processing data are reported during the post assembly phase. The elaborations provide the high edge onset corresponding to structural discontinuity assumed here as a bonding failure. Indeed, the high-density sensor network (5 mm space gap), allows to track the edge onset very precisely.

### 5.1 Fibre optic OF1

For the sake of simplicity, full steps of the SHM methodology are shown for one case, only (the rear spar); for all the others, only the output is provided, in form of the graphical interface representation. Each fibre was connected to LUNA for acquisition and the strain map was then processed by the LHEO algorithm. The readouts were graphically visualized on the lower skin image by using yellow dots to indicate the distributed sensors array, and red dots to highlight the sensors revealing a damage. In Figure 9, the after-assembly strain residuals are reported. As it can be seen, the signal output is significantly relevant, with strain values that range between about -50 and 50 microstrains. There is also a significant peak associated to the bonding transition point, as already shown in Figure 8. In the next Figure 10, the cross-correlation features as extracted by the strain map, are reported.

From these pictures, it does seem that the most remarkable edge is revealed at the egress point of the fibre; however, at a more accurate view, other minor peaks can be revealed. Now, the former ones are a known characteristic of the system, and can be neglected. The others, shall be further analysed by the LHEO algorithm to provide an expected indication of the damage presence. In fact, In the next Figure 11, the cumulative damage index (CDI) is shown all along the fibre length.

Therein, the strain signal is reported with the aim of providing a reference to the reader. As it can be seen, the egress region is clearly indicated, and other points do also emerge as indication of what the SHM code recognised as significant discontinuities. It is relevant to remind that the code aims at revealing the edges of the fault areas, and therefore it is expected that the points more easily pointed out will be their boundaries. The final picture, Figure 12, reports the same data of Figure 11, but deployed on the physical representation of the bottom skin panel to help discern the revealed points. This may be an excellent tool for the immediate comprehension by a generic user.

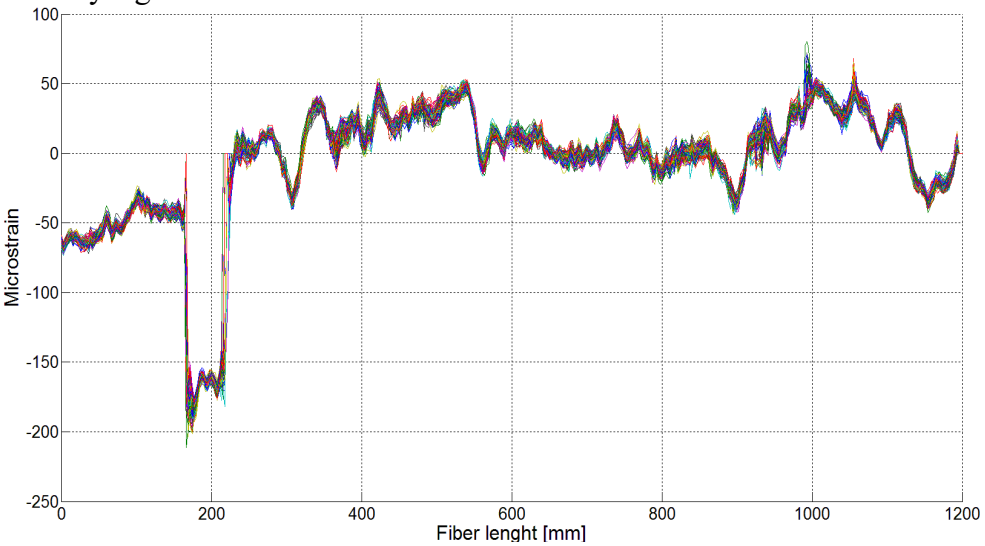


Figure 9: The residual strain after assembly for OF1 on the rear spar

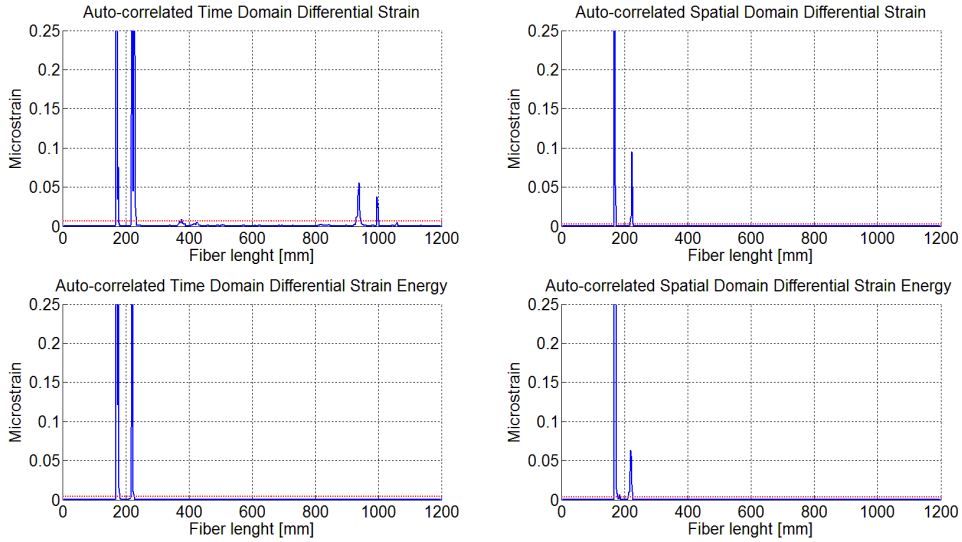


Figure 10: The cross-correlation features extracted by the strain map (phase 2, flowchart in figure 7)

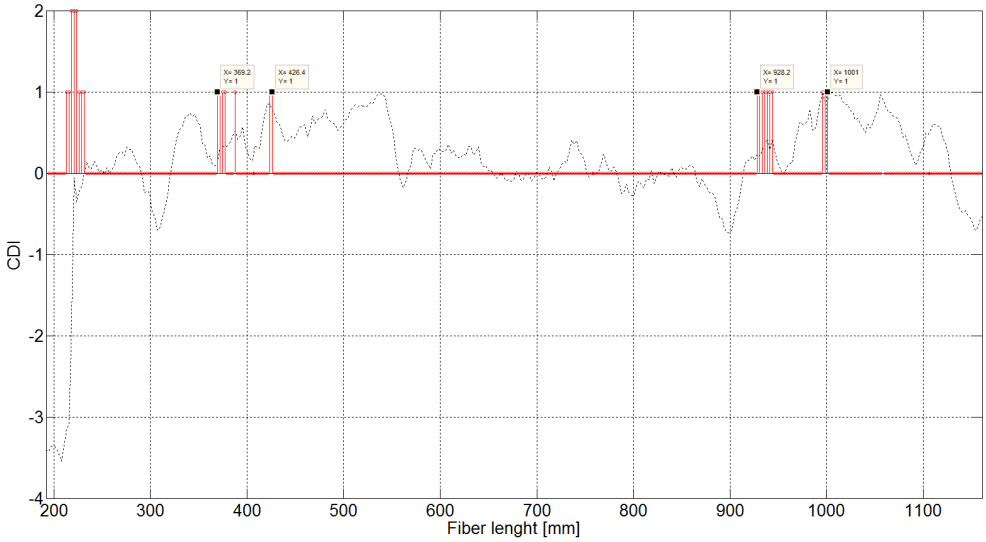


Figure 11: The cumulative damage index CDI extracted by the features (phase 3, flowchart in figure 7)

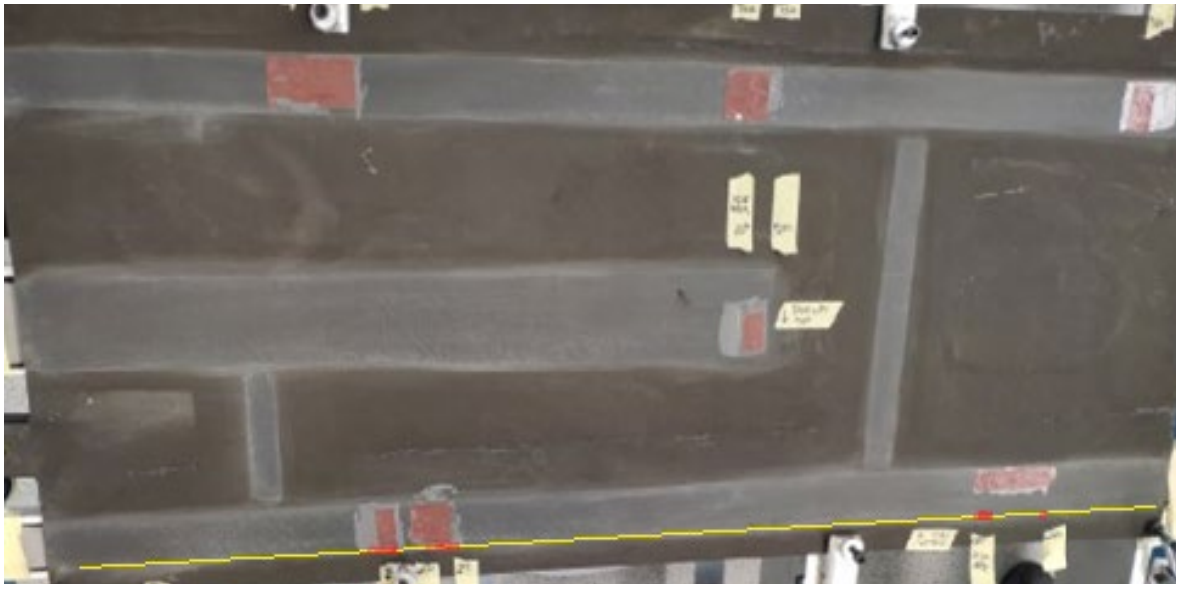

Figure 12: The graphical user interface with a representation of the fibre optic in yellow and the SHM sensors readouts indicating a damage in red

### 5.2 Fibre optic OF2

As anticipated, from this point on, it is chosen to report only the final outcomes of the data elaborations. The steps are the same, and the intermediate graphs would add only side information with respect to the algorithm capability in detecting the presence of the damage. In detail, a good proximity of the outcomes for the OF1 and OF2 may be appreciated by a comparison between Figure 12 and Figure 13. The positions of the imposed damage are clearly exhibited, and the specific prediction points are well matched. A minor discrepancy does appear at the very beginning of the fault ID.6 (Figure 4), maybe associated to a small local irregularity in the fibre deployment.

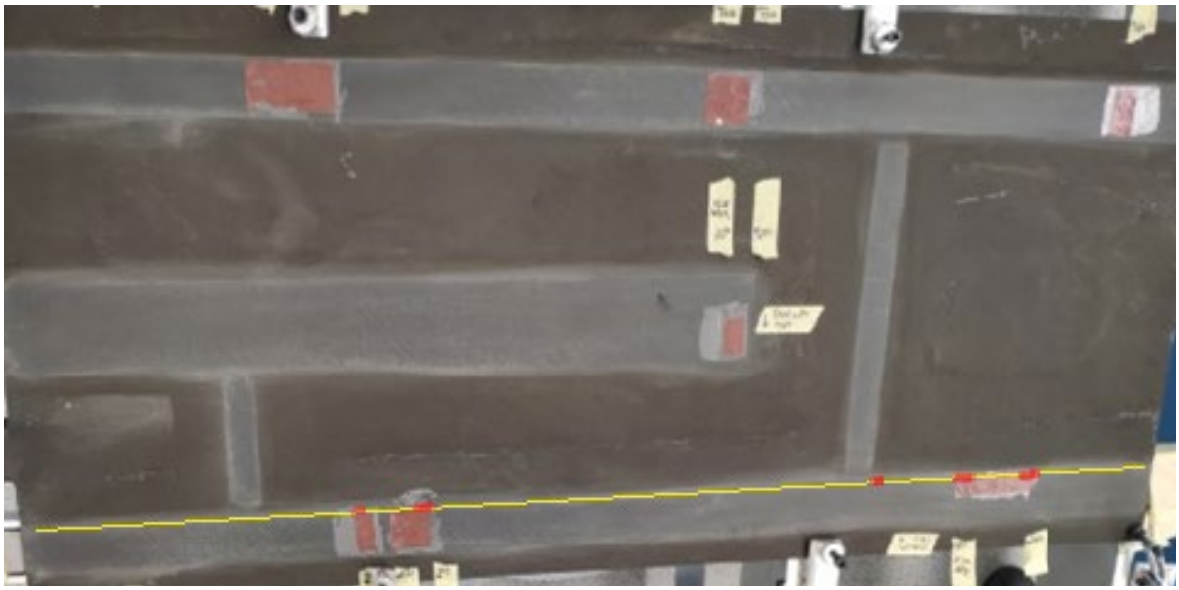

Figure 13: The graphical user interface with a representation of the fibre optic in yellow and the SHM sensors readouts indicating a damage in red

### 5.3 Fibre optic OF3 and OF4

Continuing the aforementioned tracks, in the next Figure 14 and Figure 15, the outcomes associated to the fibres deployed along the middle spars are reported. These results are particularly significant from the algorithm capability verification standpoint, since the imposed damage interested a very limited area at the tip of the central spar. Therefore, it was natural to expect that the indications could be very slight. Nevertheless, the algorithm proved to be very sensitive in this case, either, by recognizing the existence of a structural irregularity in the region of interest. This does appear very clear for the fibre OF3, while the detection for the fibre OF4 is only marginal, but nevertheless occurring at the fault edge.

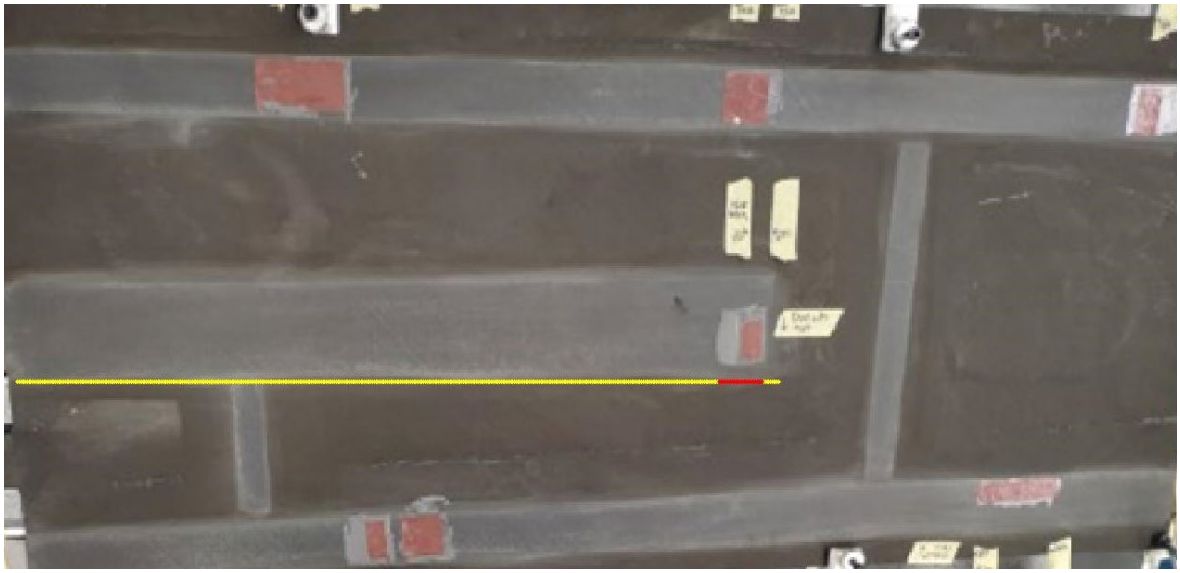

Figure 14: The graphical user interface with a representation of the fibre optic in yellow and the SHM sensors readouts indicating a damage in red

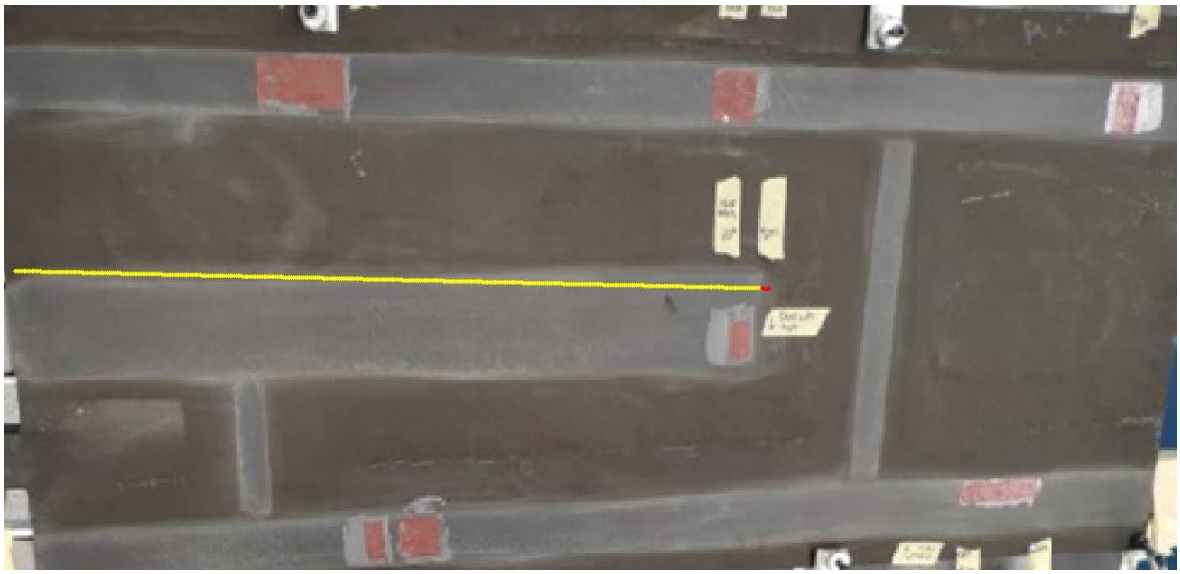

Figure 15: The graphical user interface with a representation of the fibre optic in yellow and the SHM sensors readouts indicating a damage in red

### 5.4 Fibre optic OF5 and OF6

Finally, the outcomes for the front spar are reported. Even in this case, the OF5 and OF6 are reported. The damage presence is always revealed, with a clear resolution with respect to the fibre segments that are not interested by disbonding regions; disbonding areas are always highlighted by a remarkable and homogeneous quantity of warning points. As in the other cases, few points do occur in regions nominally intact. Again, they can be explained by local irregularity in the fibre deployment or in further anomaly in the local bonding application. In the sole point of the fault ID.2, Figure 4, it could be supposed that the relevant alert shown by that sensors line, may be due to a sort of spill-over effect of the imposed damage, locally.

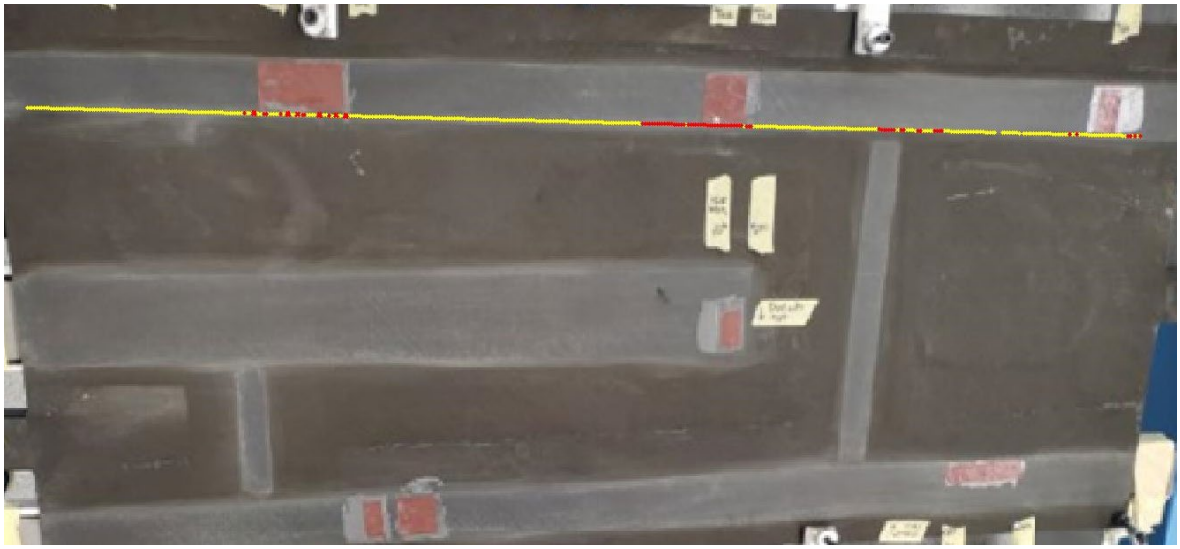

Figure 16: The graphical user interface with a representation of the fibre optic in yellow and the SHM sensors readouts indicating a damage in red.

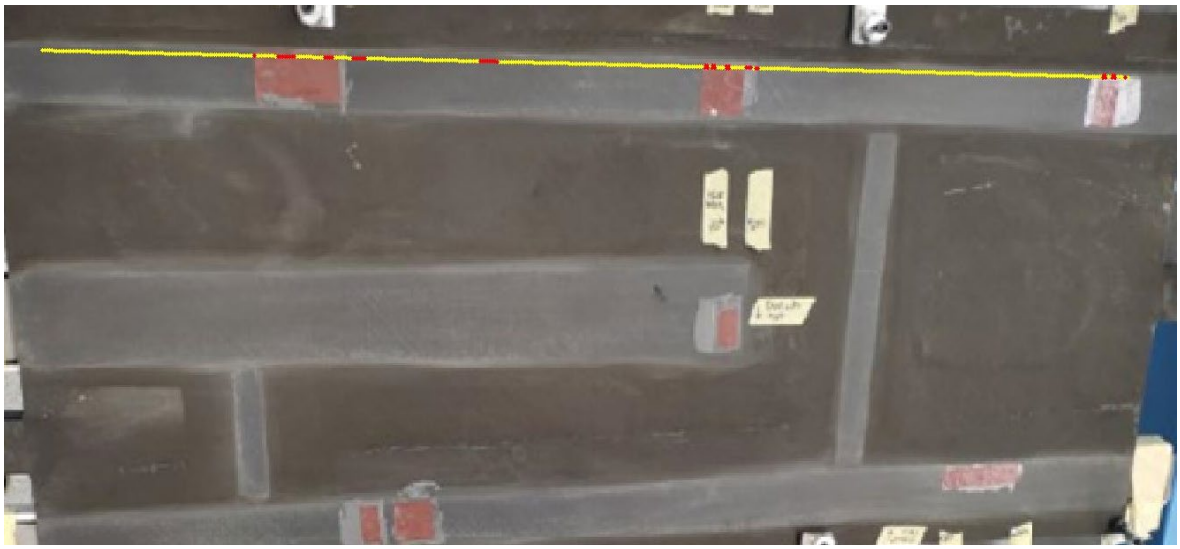

Figure 17: The graphical user interface with a representation of the fibre optic in yellow and the SHM sensors readouts indicating a damage in red.

### 5.5 Discussion

To summarise the achieved results, the following Table 1 is filled. In the table, the following parameters are reported:

- the ID for each damage (coded as in Figure 4);
- the nominal damage length;
- the estimated damage length as derived from post assembly and post installation data, respectively;
- the absolute error with respect to nominal and estimated damage length, having the nominal one as a reference.

Table 1: Estimation error for the damage length and position

| Damage ID | Nominal Damage Length [mm] | Estimated Damage Length (post assembly) [mm] | Abs Error [%] | Estimated Damage Length (post installation) [mm] | Abs Error [%] |
|---|---|---|---|---|---|
| 1 | 80 | 88 | 10 | 88 | 10 |
| 2 | 40 | 37 | 7 | 34 | 15 |
| 3 | 20 | - | - | - | - |
| 4 | 20 | 63 (ID.4+ID.5) | 21 | 112 (ID.4+ID.5) | 40 |
| 5 | 40 | | | | |
| 6 | 80 | 84 | 5 | 78 | 2 |
| 7 | 20 | 13 | 35 | 16 | 20 |

## 6 CONCLUSIONS

A first consideration must be done about the manufacturing process. It arose that the damage ID.4 and ID.5 were barely distinguished by the SHM system. The gap of 20 mm between them was probably uncovered by the adhesive during the assembly, for the excessive proximity of the two faults.

Another consideration must be done for the damage ID.3, that was scarcely revealed by the SHM system, even if a certain alert points distribution was detected; however, such a map was considered insufficient for a reasonable determination of the fault size. The partial visibility of the flaw may be associated to the fact, confirmed by the C-Scan, that the Teflon was actually arranged out of the region of interest (Figure 4).

Based on the available data (unloaded structure), the algorithm confirmed a certain capability to detect damage with:

- low amplitude strain (around 50 microstrains)
- unloaded condition; this is very important in the view of using the SHM system as a tool for NDI inspections after curing, therefore aiming at evaluating the integrity of the manufactured structural component.

Results are confirmed for both post-assembly and post-installation configuration. However,

results seem noisier for the first condition, probably due to the fact the signal-to-noise level is much higher for the absence of an external constraint, in turn inducing an additional solicitation stress with respect to the simple curing process.

Concerning faults detection, output density seems a key to be further investigated, having established the following, reasonable, priorities:

- Fault existence
- Fault quantification

It should be remarked that the nature of faults is not herein considered, and that the errors are generally around 25%, a feature that can be widely acceptable at this stage even considering that the damage effect extension is usually wider than its actual size.

A final point concerns the need of investigating the presence of undesired anomalies along the fibre length, in regions where the structure is considered nominally integral, in this investigation. These false positives could be attributed to irregular fibre deployment, or to local structural imperfections, for instance. In the first case, it pushes the technology for the development of automated fibres placement, while in the second case it urges to perform non-trivial post-test inspections to verify the possible existence of supposed anomalies (then strengthening the algorithm capability) or other motivations for the issue of such unexpected alerts.

## ACKNOWLEDGMENTS

The authors want to thank all Piaggio laboratory staff, and particularly Mrs. L. Bosco and Mr. D. Cirio, for their support during the preparation and execution of the tests. A special acknowledgment to Mr. A. Cozzolino, for his continuous support, and strategical orientation to this research activity. Further the authors wants to remember that the activities described in this paper have been funded by the program CLEAN SKY2 within the AIRFRAME ITD (Integrated Technology Demonstrators) framework that is the most important aeronautical research program of the European Community.

## REFERENCES

[1] Ewald, V.; Groves, R.; Benedictus, R. Transducer Placement Option for Ultrasonic Lamb Wave Structural Health Monitoring (SHM) on Damage Tolerant Aircraft Substructure. 11th International Workshop on Structural Health Monitoring (IWSHM) 2017: Real-Time Material State Awareness and Data-Driven Safety Assurance, Vol. 2, pp. 1811-1818. Stanford (USA), 12-14 September 2017. https://doi.rog/ 10.12783/shm2017/14063.

[2] Boller, C. Implementation Strategies for SHM in Civil and Military Applications. In: Structural Health Monitoring of Military Vehicles. Suleman, A. (Ed), STO-EN-AVT-220. STO Educational Notes, NATO Science & Technology Organization, 2014.

[3] Acellent. Localized ("Hot Spot") Monitoring. Available at https://www.acellent.com/applications/localized-monitoring. Last accessed May 27th, 2023.

[4] Datta, A.; Augustin, M.J.; Gaddikeri, K.M.; Viswamurthy, S.R.; Gupta, N.; Sundaram, R. Damage detection in composite aircraft wing-like test-box using distributed fibre optic sensors. Optical Fibre Technology, 2021; 66, 102651. https://doi.org/10.1016/j.yofte.2021.102651

[5] Monica Murthy, N.; Desai Kakade, P. Review on Strain Monitoring of Aircraft Using Optical Fibre Sensor. International Journal of Electronics and Telecommunications, 2022; 68, 3, 625-34. https://10.24425/ijet.2022.141282.

[6] De Martin, A.; Sorli, M.; Jacazio, G. Integrated Health Monitoring for Robust Actuation System of UAV Primary Flight Controls. Int. J. Mech. Control 2019, 91–104.

[7] Kressel, I.; Dorfman, B.; Botsev, Y.; Handelman, A.; Balter, J.; Pillai, A.C.R.; Prasad, M.H.; Gupta, N.; Joseph, A.M.; Sundaram, R.; et al. Flight Validation of an Embedded Structural Health Monitoring System for an Unmanned aerial Vehicle. Smart Mater. Struct. 2015, 24, 075022–075030.

[8] Fernandez, A.; Menendez, J.; Guemes, A. Damage detection in a stiffened curved plate by measuring differential strains. In Proceedings of the 16th International Conference on Composite Materials, Kyoto, Japan, 8–13 July 2007.

[9] Ciminello, M.; Concilio, A.; Galasso, B.; Pisano, F.M. Skin–stringer de-bonding detection using distributed dispersion index features. Struct. Health Monit. J. 2018, 17, 1245–1254. https://doi.org/10.1177/1475921718758980.

[10] Concilio, A.; Ciminello, M.; Galasso, B.; Pellone, L.; Mercurio, U.; Apuleo, G.; Cozzolino, A.; Kressel, I.; Shoham, S.; Bardenstein, D. De-Bonding Numerical Characterization and Detection in Aeronautic Multi-Element Spars. Sensors 2022, 22, 4152. https://doi.org/10.3390/s22114152.